Extracellular Matrix-Liposomes: A Novel Vehicle for Tissue Regenerative Wound Healing

Keel Yong Lee
Harvard University https://orcid.org/0000-0002-7204-3822
Huong Nguyen
Sogang University
Agustina Setiawati
Sogang University
So-Jung Nam
Sogang University
Minyoung Kim
Sogang University
Il-Gyu Ko
Kyung Hee University
Won Hee Jung
Chung-Ang University
Kevin Kit Parker
Harvard John A. Paulson School of Engineering & Applied Sciences https://orcid.org/0000-0002-5968-7535
Chang-Ju Kim
Kyung Hee University
Kwanwoo Shin (kwshin@sogang.ac.kr)
Sogang University https://orcid.org/0000-0002-7563-8581

Article

Keywords: extracellular matrix-liposomes, wound healing, tissue regeneration

Posted Date: April 8th, 2021

DOI: https://doi.org/10.21203/rs.3.rs-302194/v1

Abstract

The unfolded states of fibronectin (FN) subsequently induce the formation of the extracellular matrix (ECM) fibrillar network, which is necessary to generate new substitutive tissues. Here, we demonstrate that negatively charged small unilamellar vesicles (SUVs) qualify as candidates for FN delivery due to their remarkable effects on the autonomous binding and unfolding of FN, which leads to increased tissue regeneration. *In vitro* experiments revealed that the FN-SUV complex remarkably increased the attachment, differentiation, and migration of fibroblasts. The potential utilization of this complex *in vivo* to treat inflammatory colon diseases is also described based on results obtained for ameliorated conditions in rats with ulcerative colitis (UC) that had been treated with the FN-SUV complex. Our findings provide a new ECM-delivery platform for ECM-based therapeutic applications and suggest that properly designed SUVs could be an unprecedented FN-delivery system that is highly effective in treating UC and other diseases.

Main

Fibronectin (FN) plays an essential role in the wound healing process due to its ability to form an extracellular matrix (ECM) and to regulate cellular activities[1]. In addition to the ability to bind together and form FN fibrils, FN molecules have various recognition and binding sites in their structure, and these sites favor interactions with various cell types, growth factors, cytokines, and other ECM proteins, such as collagen, laminin, and heparin[2, 3, 4]. Soluble FN is a folded dimeric protein whose subunits are composed of three types of repeating modules, I, II and III, which are variably expressed due to alternative splicing of RNA[5]. Among the three modules, FN type III (FNIII) is the largest and most common repeat[2, 4]. Once in contact with the cell surface, FNIII domains will be recognized by integrin proteins on the cell membrane and subsequently undergo an unfolding process caused by cell-traction forces, which induces FN fibrillogenesis[3, 6]. Unfolding is, therefore, essential in FN functionalization, which is the target of FN-based material fabrication[1, 7]. Although the cell binding sites within the FNIII module are exposed on the surface, the active domains, which are known to be phosphorylation sites, are usually hydrophobic. These domains are buried within FNIII modules in the folded state due to hydrophobic interactions and are maintained by intramolecular ionic bonds[8, 9]. Therefore, unfolding FN is crucial not only for enhancing the elasticity of fibronectin fibrils but also for exposing the buried sites that are known to display enzymatic activities and to regulate many cellular activities[10].

The use of soluble, compact FN has been successful in improving wound-healing treatments. Some examples of wounds considered thus far are diabetes- and radiation-induced cutaneous wounds in rats or mice[11, 12]. Corneal epithelial wounds have also been reported to heal more quickly after having been treated using eye drops containing a soluble FN and hyaluronan combination[13]. Nevertheless, recent reports have revealed that supplying cells with unfolded FN, compared to compact FN, improves the wound-healing efficiency more remarkably. For example, Phong *et al.* reported an enhanced formation of FN fibrils after denaturation of FN by using urea, leading to improved platelet adhesion[14]. In 2018,

Christophe *et al.* adopted rotary jet spinning to produce unfolded FN fibers and confirmed that its use effectively enhanced wound healing[15]. These studies suggest that for higher wound-healing efficiency, FN used in tissue regeneration should undergo certain procedures to induce changes in its conformation. Some methods for doing so include physical binding on different substrates, modifying surfaces with chemical groups, or using gold nanoparticles[16, 17, 18, 19]. Although unfolded FN has been proven to have improved functions over compact FN, the methods for unfolding FN that have been reported so far have had limited clinical applications due to the complex processes required for the fabrication and chemical modification of the substrate.

In this study, to tackle the above issues, we demonstrate a potential FN-unfolding platform using negatively charged, small unilamellar vesicles (SUVs) for FN delivery. These SUVs are simply produced by using a unique composition of lipids so that the surface of the SUV not only enhances direct binding but also induces the unfolding of FN. The effects of FN delivered by our SUV system were investigated using a variety of cell-based assays to evaluate all aspects of cellular activities, including growth, differentiation, and migration. An *in vivo* wound-healing model of ulcerative colitis (UC) was adopted to evaluate the sufficiency of the unfolded FN that was delivered. Collectively, our findings indicate that negatively charged SUVs represent a new platform for functional FN delivery.

For critical cellular functions to be accessed, compact FN must be unfolded to expose buried domains[20]. Hence, our first effort was to determine the composition of lipids that not only enhanced the binding efficiency of FN but also induced conformational changes of FN prior to its delivery to cells (Fig. 1a). The optimized lipid composition of SUVs was found to be zwitterionic:net negative:cholesterol at a ratio of 3:2:1. An appropriate ratio of 1,2-dioleoyl-sn-glycero-3-phospho-L-serine (DOPS) resulted in a net negative charge on the surface of the SUV. The negatively charged SUVs had strong interactions with FN compared to those with only zwitterionic lipids (Fig. S1). An analogous giant unilamellar vesicle (GUV) system was developed with the same lipid composition but a hundredfold increase in size (20-30 μm on average) (Figs. 1b and c). The analogous GUVs allowed us to directly observe the binding by using confocal imaging. FN tended to form insoluble aggregates when it was incubated with neutral vesicles (Fig. 1b) but was attached evenly on the surfaces of negatively charged GUVs (Fig. 1c). The strongly favorable and selective binding of FN to a negatively charged lipid is obvious in phase-separated GUVs with two lipid phases (Fig. S1a). The liquid order (L_o) phase contained zwitterionic sphingomyelin, and the liquid disorder (L_d) phase contained DOPS and other unsaturated lipids, constructing the negative portion of the membrane. Under the same experimental conditions, FN was observed only in the L_d phase (green fluorescence) and not in the L_o phase of the same GUV (Fig. S1b). This result clearly confirmed that a negatively charged vesicle system selectively enhanced FN binding.

Evaluating the binding of FN on SUVs with an appropriate size for cell delivery was much more sophisticated because SUVs (average radius of 200 nm) are remarkably smaller than GUVs (average radius of 20 μm). Images obtained from cryogenic transmission electron microscopy (Cryo-TEM) showed that the SUVs incubated with FN had a membrane that was significantly thicker (thickness d = 8.3 ± 0.6

nm) than the membrane containing only lipids (d = 4.4 ± 0.6 nm) (Figs. 1d and e). The thickness of the membrane comprises the lipid membrane itself, which is approximately 4-5 nm, and an additional FN layer, if any, on the membrane. Therefore, this result implied that FN indeed bound to the SUVs, which was observed as an increase in the membrane thickness. In addition to performing single-SUV thickness measurements, we measured the size distribution of the entire SUV population by using the dynamic light scattering (DLS) method (Fig. S2). The results showed that the average size of the SUV population increased from 140.3 nm to 178.3 nm and that the curve shifted to the right (larger size), indicating that the size of the SUV had increased after incubation in an FN solution.

In addition to enhancing the binding of FN on the surface, negatively charged SUVs induced conformational changes. The stretching of FN was measured by using fluorescence resonance energy transfer (FRET) with FN labeled with donor-acceptor dyes (FN-DA). Four molar (4 M) guanidinium chloride (GdnHCl), one of the strongest denaturants, was used as a positive control [21] (Fig. S3). Figure 1f shows that the I_A/I_D ratio of FN-DA incubated with SUVs was comparable to that of FN-DA incubated in 4-M GdnHCl (0.38 ± 0.06 and 0.34 ± 0.13, respectively) and was significantly lower than that of FN-DA incubated in phosphate buffered saline (PBS) used for SUV hydration or sucrose used for GUV hydration (1.18 ± 0.2 and 1.19 ± 0.05, respectively). FRET was also accomplished on GUVs coated with FN-DA; the I_A/I_D ratio of FN-DA was lower after incubation with GUVs (from 0.92 ± 0.11 to 0.18 ± 0.06 after incubation) (Figs. 1g and h). This result verified that stretching of FN had also occurred on the surfaces of GUVs. Taken together, the negatively charged SUV system is a suitable vehicle for delivering FN in an active, unfolded conformation.

FN has been utilized in cell and tissue cultures to strengthen cell attachment, proliferation, and migration[17, 19, 22, 23, 24]. We hypothesized that the conformational changes induced by binding to negatively charged SUVs would enhance the above cellular functions of FN to a greater extent than its compact form. We performed *in vitro* experiments using human neonatal dermal fibroblast (HDFn) cells, as they play essential roles in tissue repair. The fate of FN after having been delivered to HDFn cells was probed with either green (FN-SUV) or red (FN) fluorescent indicators. In both groups, FN fibrils were found to colocalize with their membrane receptor, integrin α5 (Fig. 2a). However, more FN fibrils were produced when FN was delivered by using SUVs. We found an interesting event in which a clump of FN-SUVs rapidly burst and expanded when it came into contact with the HDFn cell surface (Fig. 2b). This event was not observed when using FN without SUVs (data not shown), indicating that SUVs promoted the interaction of FN with the cell surface. As we observed that SUVs unfolded FN in advance of the interaction with the cell membrane, we predicted that this process would subsequently increase the adhesion of cells to the culture substrate. Fig. 2c shows that trypsinized HDFn cells had limited attachment to the culture dish. However, when delivered by using the FN-SUV system, the number of active fibroblasts (seen as spindle-shaped cells with long lamellipodia) increased significantly[25]. A quantitative comparison of cell attachment among the experimental groups was performed by calculating the total area of attached cells, as shown in Fig. 2d and Video S4. Moreover, the total cell surface area covered by FN was significantly higher when FN was delivered by SUV, implying enhanced

FN binding to the cells (Fig. 2e). Although FN promoted cell attachment, stretched FN made the surfaces of GUVs unfavorable for bacteria, particularly Staphylococcus aureus (*S. aureus*), an organism that often causes opportunistic infections on skin and leads to tissue damage, as described in a previous study[26]. *S. aureus* was incubated with different types of GUVs (Fig. S4). A large number of bacteria (white) were found on collagen-coated GUVs (COL-GUVs). In contrast to the case with the bare lipid GUVs, the bacteria were hardly present on the FN-coated GUVs, suggesting that using the stretched FN as a wound healing agent had advantages in preventing unwanted bacterial infection.

When tissue is wounded, released cytokines attract fibroblasts from the surrounding area[1]. During this time, fibroblasts are activated and migrate towards the wounded area with the recruitment of ECM proteins including FN[27, 28]. We tested whether the stretching of FN would promote the migration rate of fibroblasts, as it has been shown to enhance ECM formation. Figure 3a shows representative images cut from Videos S5-7, illustrating the movements of HDFn-GFP cells as a function of time. Single cells were tracked, and the average migration speeds (μm/min) were compared among groups. As we expected, the migration speed increased when SUVs (green circles) were used for FN delivery (Figs. 3a and b). This enhancement may result from the formation of a denser FN matrix, which facilitates cell adhesion and migration. The expansion of the FN matrix among groups over time can be seen clearly in Fig. S5 and Video S11.

In vitro scratch assays were used to assess the cell migration speed to evaluate cell migration[29]. To ensure the reproducibility of the experiments, we set up an incubation chamber in the confocal microscope system and continuously observed a specific wounded area for at least 16 h. Representative images at 0 h and 12.5 h for each group are shown in Fig. 3c; the corresponding time-lapse images are shown in Videos S8-10. The results revealed that among the experimental groups, the gap closed at the highest rate in the FN-SUV-treated group, with 60.3 ± 4.3 % of the gap area being covered by HDFn cells after 15 h compared to only 33.5 ± 4.2 % in the FN-treated group (Fig. 3d). Insignificant proliferation among all groups was observed during the first 24 h, which showed that the cell migration assays were unbiased, with minimal contribution from cell proliferation (Fig. S6).

The healing effects of FN *in vivo* have been described previously by using a wide range of wound models in different species, such as rabbits, mice and guinea pigs[12, 30, 31]. Existing evidence from previous studies indicates that in inflammatory bowel-related diseases, such as ulcerative colitis (UC) and Crohn's disease, the level of FN in the plasma is decreased significantly[7, 32, 33]. In this present study, the healing performance of FN-SUVs was further assessed *in vivo* using an UC model for rats. An approved protocol using 4% acetic acid was applied to induce UC in the colon, followed by a 10-day treatment strategy with either FN or FN-SUVs (Fig. S7). After treatment, the entire colons of the rats were removed to compare changes in morphology, wet weight and various tissue damage markers. As shown in Fig. 4a, the FN-SUV-treated group showed remarkably thinner and smoother colon walls with less mucus (less tissue damage) than the FN-treated group. In addition, FN-SUV-treated colons had significantly lower wet

weights than those treated with FN alone, indicating that SUV-FN treatment reduced inflammation and swelling in the colons.

Colon tissues after either FN or FN-SUV treatment were further analyzed semi-quantitatively for inflammatory markers, including tumor necrosis factor (TNF)-α, interleukin (IL)-1β, IL-6, cyclooxygenase (COX)-2 and inducible nitric oxide synthase (iNOS). However, the differences in the levels of TNF-α, IL-1β, and IL-6 expression between the FN and FN-SUV groups were insignificant (Fig. S8), whereas COX-2 and iNOS expression was downregulated in rats treated with FN-SUV, suggesting that the unfolding of FN via the SUV may expose the domains that communicate with cells via these two pathways (Figs. 4a and b)[34, 35]. The inhibition of COX-2 and iNOS expression in our *in vivo* model clearly showed that inflammation was effectively decreased in the experimental UC model when the FN-SUV treatment was administered[36].

Many attempts have been made to unfold FN prior to it reaching the cell. However, an appropriate approach to unfolding FN for tissue regeneration applications is still a challenge. The unfolding of FN requires the breakage of intramolecular bonds and hydrophobic interactions, which can be induced by using either chemicals[14, 21] or mechanical forces[8, 15]. The pH or salt concentration can induce the stretching of FN, but this reversible change is hard to maintain for cell delivery, and the solution must be similar to the physiological environment. The improper removal of a denaturant will otherwise potentially result in negative effects on live cells and tissues[21].

The adsorption and unfolding facilitated by chemical modifications raise a risk of cytotoxicity[16, 17, 18, 19]. On the other hand, approaches using mechanical forces to unfold FN usually exploit solid substrates and polymers with low biocompatibility. The most promising approach might be to produce nanofibers from soluble FN by using mechanical forces[15, 37]. However, FN nanofiber production remains challenging, as the use of the fabrication technique may not always be possible in laboratories. Nonetheless, FN nanofibers are more appropriate for dressing materials and cutaneous wound treatment than for the treatment of bowel diseases. Despite major efforts to deliver ECM or FN to damaged tissues via surface-modified substrates, the fabrication of these materials remains very complex, and these substrates usually have to be removed from the body after having been applied, which is not appropriate for deep, closed wounds[38, 39]. In contrast, negatively charged SUVs are composed of phospholipids and cholesterol, which are highly biocompatible and have negligible cytotoxicity[40]. Accordingly, in our novel system, we managed to develop a negatively charged SUV system that has negligible toxicity[40, 41]. In addition, the preparation of self-assembled SUVs in aqueous solution followed by the autonomous binding and unfolding of FN was much simpler and afforded higher yields than any other method.

The adsorption and unfolding of FN on liposomes were once reported by Micheal *et al.* as an enhanced drug delivery approach using liposomes that can avoid the rapid uptake of the reticuloendothelial system[42]. Both gel-phase and liquid-phase liposomes were considered for FN selective binding, and only liposomes composed of lipids that had high melting temperature (T_m) or existed in the gel phase at room temperature, such as DPPC (T_m = 41°C) or DSPC (T_m = 55°C), were observed to bind and unfold FN[42].

Interestingly, we have sufficient experimental evidence to prove that FN is able to bind and unfold on liquid-phase SUVs composed of lipids with T_m < 0°C under the condition that a negatively charged lipid (DOPS) is added. Due to the low T_m values of the lipids used, the fabrication of negatively charged SUVs is simplified and can be performed at room temperature. Thus, the negatively charged SUV system has significant advantages over previously used materials in terms of fabrication, cytotoxicity, and biocompatibility.

Collectively, we confirmed that a negatively charged SUV can effectively unfold FN bound to its surface. Subsequently, the SUVs enhanced the effects of FN on HDFn migration and proliferation. *In vivo* experiments showed that rats with UC that had been treated with FN-SUVs improved faster than rats treated with only soluble FN. The abundant amount of FN in the plasma is an advantage of using FN as a potential tissue regeneration material[1, 7, 32]. FN also possesses an exceptional property for wound healing, as stretched FN disrupts the binding of *S. aureus,* a common cause of infections in humans[26].

We conclude that negatively charged SUVs are ideal vehicles for functional FN delivery. The system shows the capability to carry and unfold FN with high biocompatibility and safety and can be used as a platform for protein-small molecule drug incorporation, especially for drugs that accelerate wound healing. Further studies are expected to discover the mechanisms underlying the efficacy of the SUV-FN delivery system.

Methods

Preparation of small unilamellar vesicles (SUVs) with negatively charged surfaces

Multilamellar liposomes were first prepared by blending DOPC:DOPE:DOPS:cholesterol in a ratio of 2:1:2:1 to make a mixture with a total concentration of 5 mg of lipids per ml. One milliliter of the lipid blend in a black glass vial was blown dry using N_2 gas for 2 h to completely remove the solvent. The dried lipids were then rehydrated with 1X PBS (pH 7.4) by using a vortex mixer at room temperature for 60 minutes. The lamellarity of the liposomes was reduced by using 5 cycles of freezing in liquid nitrogen and thawing in a water bath at 40°C to break down the outer bilayers. Finally, the vesicles underwent extrusion by using a mini-extruder set (Avanti, Inc) to pass them through a 200-nm membrane filter 11 times.

Preparation of giant unilamellar vesicles (GUVs)

A lipid mixture with a composition of either DOPC:DOPE:DOPS:cholesterol (2:1:1:1 molar ratio) for negatively charged GUVs or DOPC:DOPE:cholesterol (2:1:1) for neutrally charged GUVs was prepared at a concentration of 1 mg/ml. Approximately 30 µl of the lipid mixture was deposited on ITO glass (30-Ohm sheet resistance) and quickly dried by using flowing N_2 gas. The lipids were continuously dehydrated in a vacuum desiccator for approximately 1 h. A silicon ring with a thickness of 1 mm was inserted between two ITO glass slides to make space for a hydrate solution. For observations under a light microscope, the

lipids were rehydrated with an inner solution containing 200 mM sucrose and 2 mM MES (pH 4.2) and were later diluted with an outer solution containing 200 mM glucose and 2 mM MES (pH 4.2). A fibronectin (FN) solution that had been previously diluted in deionized water was added to make an FN-GUV solution at a final concentration of 10 µg/ml, followed by incubation at 37°C overnight before performing confocal microscopy.

FN conjugation for fluorescence resonance energy transfer analysis

Fibronectin (FN) was subsequently labeled with Alexa-546 C5 maleimide on its cysteine residues and with Alexa-488 NHS succinimidyl ester on its lysine residues. Lyophilized FN diluted with PBS to a concentration of 1 mg/ml was denatured in the chaotropic agent guanidine hydrochloride (GdnHCl, 8 M) at a ratio of 1:1 (v/v) and incubated with Alexa 546 maleimide at a molar ratio of 1:30. Excess fluorescence dye was removed through dialysis by using a slide-A-lyzer dialysis cassette with a 10,000 Dalton MW cut-off in 0.1 M sodium bicarbonate ($NaHCO_3$) at pH 8.5. The buffer was changed twice every two hours before being stored overnight at 4°C. The initial conformation of labeled FN was confirmed using spectrofluorometry. Afterwards, the labeled FN was incubated for one hour with Alexa 488 NHS succinimidyl ester at a ratio of 1:70 (mol/mol). Doubly labeled FN with a donor and an acceptor dye (FN-DA) was separated from the free dyes by using a PD-10 column (pre-equilibrated with PBS). The ratio of the donor intensity to the acceptor intensity per FN dimer (I_A/I_D) was determined by measuring the fluorescence of FN-DA at 280, 496, and 556 nm. For long-term storage, FN-DA was stored in 10% glycerol at -80°C.

Characterization of FN-SUV incorporation by using cryogenic transmission electron microscopy (cryo-TEM)

FN was incubated overnight with preformed SUVs at a ratio of 1:5 (*w/w*). Immediately after incubation, samples of either SUVs or FN-SUVs were preserved by vitrification and supported by Quantifoil (R 2/2, 400-mesh holey-carbon grid, Quantifoil Micro Tools). Vitrified samples were prepared by applying a 3-µL drop of sample suspension to a cleaned grid, blotting away the excess with filter paper, and immediately plunging the grid into liquid ethane. Grids were stored under liquid nitrogen until transferred to the transmission electron microscope for imaging. Electron microscopy was performed using a Talos L120C electron microscope (FEI, Hillsboro, OR, USA) operating at 120 kV. Vitreous ice grids were transferred into the electron microscope by using a cryostage that maintained the grids at a temperature below -170°C. An image of each grid was acquired on multiple scales to assess the overall distribution of the specimen. Images were collected using a 4k × 4k Ceta CMOS camera at a search magnification of 5000 and a final magnification of 29,000 to 280,000 at an underfocus of ~ 2.5 µm. After potentially suitable target areas for imaging at lower magnifications had been identified, pairs of highly magnified images were acquired using the UI V1.6 Talos software. ImageJ software was used to analyze the intralamellar distances in the original, high-resolution images collected using the microscope (4096 × 4096 pixels).

Fluorescence resonance energy transfer (FRET) analysis

The fluorescence intensity of FN-DA was measured using a standard fluorescence spectrophotometer (Hitachi F-7000) with excitation of the donor at 488 nm. The positive controls were measured using a series of GdnHCl concentrations from 0 to 4 M. The FRET measurement over a range of denaturant concentrations was used to plot the correlation of the FRET efficiency with the degree of FN unfolding. FN-DA was incubated overnight with preformed SUVs at a ratio of 1:5 (w/w) with gentle rocking to enhance the binding. Then, cryo-TEM and FRET were exploited to characterize the incorporation and unfolding of FN on the SUVs. The background fluorescence was measured using SUVs in solution, and the negative control was measured using FN-DA in PBS without SUVs at the same concentration as in the FN-SUV sample.

Colocalization, attachment area and fibril formation imaging

HDFn cells were cultured in DMEM (FBS 10%, 1% Pen-Strep). For integrin observation, FITC-conjugated integrin 5 antibody was used. FN was diluted in PBS and used at a concentration of 10 μg/ml. For cell attachment experiments, HDFn-GFP cells were detached using trypsin-EDTA when the confluence had reached 80% and were then transferred to a new culture dish, treated with non-labeled FN and imaged every hour in an on-stage incubator. For quantification of the area of the FN fibrils, HDFn-GFP cells were treated with lissamine-rhodamine-labeled FN and imaged for 25 min.

In vitro scratch assay

In migration experiments, GFP-HDFn cells were cultured in T75 flasks to reach a confluence of 80-90% and were then transferred to 35-mm dishes for continuous culturing over 24 h with 10% FBS for attachment. When cells had formed a confluent monolayer, the medium was replaced with low-serum DMEM (0.4% FBS) every 24 h to minimize the effects of proliferation on the migration speed and to avoid unexpected apoptosis[43]. The distance that a single cell moved was tracked using ImageJ.

A scratch mimicking a wound was created using a p200 pipette tip by scraping a straight line across the center of the dish. Cell debris was then washed away gently with 2 ml of low-serum medium before being supplemented with FN-SUV. The 35-mm dish was placed in a stage-top incubator (Zeiss, USA) with a CO_2 supply and a controlled temperature of 37°C to obtain the same optical field during the image acquisition. Images of GFP-HDFn cells migrating to the scratch were recorded using confocal microscopy (ZEISS LSM 710, USA) in time series mode at 1-hour intervals for at least 15 h.

Ulcerative colitis rat model

We followed the Guidelines for the Care and Use of Animals approved by the National Institute of Health Council for the management and use of animals for laboratory tests. The experimental design was approved by the Institutional Care and Use Committee of Kyung Hee University (KHUASP(SE)-15-085). Rats were divided into the following five groups (n = 10 in each group): healthy group (negative control), ulcerative colitis (UC)-induced group (positive control), UC-induced/mesalamine-treated group, UC-induced/FN-SUV-treated group, and UC-induced/FN-treated group.

Induction of ulcerative colitis by using acetic acid

Ulcerative colitis (UC) was induced by using acetic acid, as previously described[44]. The rats were anesthetized with Zoletil 50® (10 mg/kg; Vibac Laboratories, Carros, France). Animals were fasted for 48 h for UC preparation. A stainless-steel feeding needle (round tip, 16 gauge) was then carefully inserted into the colon of a rat with the tip being 8 cm proximal to the anus. Then, 4% acetic acid (Sigma Chemical Co., St. Louis, MO, USA) in 0.9% saline (1.0 ml) was injected into the lumen of the colon. The control group underwent intracolonic injection with saline instead. The rats were maintained in a supine Trendelenburg position for 5 min to prevent leakage of the injected acetic acid solution.

UC Treatment

The treatments were administered three days after acetic acid injection. The dosages for the groups were as follows: mesalamine (4 g/100 ml, Asacol Enema, Tillotts Pharma, AG, Swiss), FN-SUVs (20 μg/ml FN, 100 μg/ml SUVs), and FN (20 μg/ml). For drug administration, the rats were confined in an acrylic cylinder (diameter: 6 cm, length: 20 cm, height: 10 cm) without anesthesia. A stainless-steel feeding needle (round tip, 16 gauge) with a syringe was then carefully inserted through the anus into the damaged site. Then, each drug (1.0 ml) was injected into the lumen of the colon once a day for 10 days after induction of UC.

Western blotting

Colon tissues were homogenized on ice, lysed with lysis buffer, and then centrifuged at 14,000 rpm for 30 min. The amount of protein in each sample was quantified using a Bio-Rad colorimetric protein assay kit (Bio-Rad, Hercules, CA, USA). Sodium dodecyl sulfate-polyacrylamide gels were used to separate proteins (30 μg), after which the separated proteins were transferred onto nitrocellulose membranes. Goat COX-2 antibody (1:1000; Santa Cruz Biotechnology, Santa Cruz, CA, USA), mouse iNOS antibody, and mouse β-actin antibody (1:1000; Santa Cruz Biotechnology) were used as the primary antibodies. Horseradish peroxidase-conjugated anti-mouse antibodies (1:2000; Vector Laboratories, Burlingame, CA, USA) for iNOS, β-actin, and COX-2 were used as secondary antibodies. Membrane transfer was conducted at 4°C by using a cold pack and prechilled buffer. An enhanced chemiluminescence (ECL) detection kit (Santa Cruz Biotechnology) was used for band detection. Molecular Analyst™ (version 1.4.1, Bio-Rad) was used to analyze the detected bands.

Declarations

Funding

This work was supported by Samsung Science and Technology Foundation under Project Number SSTFBA180112010.

Author contributions

K.Y.L. and H.T.N performed live cell imaging, cell migration and proliferation assays. A.S. performed FRET. S.J.N and M.K. performed cryo-TEM experiment. I.G.K and W.H.J. performed in vivo experiments. K.K.P, C.J.K. and K.S. designed and supervised experiments. K.Y.L, H.T.N and K.S. designed the study and wrote the manuscript.

Competing interests

The authors declare no conflict of interests to any institution or company.

Data and materials availability

All data is available in the main text or the supplementary materials.

References

1. To WS, Midwood KS. Plasma and cellular fibronectin: distinct and independent functions during tissue repair. *Fibrogenesis Tissue Repair* **4**, 21 (2011).
2. Gao M, Craig D, Vogel V, Schulten K. Identifying unfolding intermediates of FN-III(10) by steered molecular dynamics. *J Mol Biol* **323**, 939-950 (2002).
3. Lemmon CA, Weinberg SH. Multiple Cryptic Binding Sites are Necessary for Robust Fibronectin Assembly: An In Silico Study. *Sci Rep* **7**, 18061 (2017).
4. Gee EP, Yuksel D, Stultz CM, Ingber DE. SLLISWD sequence in the 10FNIII domain initiates fibronectin fibrillogenesis. *J Biol Chem* **288**, 21329-21340 (2013).
5. Maurer LM, Ma W, Mosher DF. Dynamic structure of plasma fibronectin. *Crit Rev Biochem Mol Biol* **51**, 213-227 (2015).
6. Schwarzbauer JE, Sechler JL. Fibronectin fibrillogenesis: a paradigm for extracellular matrix assembly. *Curr Opin Cell Biol* **11**, 622-627 (1999).
7. Verspaget HW*, et al.* Assessment of plasma fibronectin in Crohn's disease. *Hepatogastroenterology* **38**, 231-234 (1991).
8. Smith ML*, et al.* Force-induced unfolding of fibronectin in the extracellular matrix of living cells. *PLoS Biol* **5**, e268 (2007).
9. Johnson KJ, Sage H, Briscoe G, Erickson HP. The compact conformation of fibronectin is determined by intramolecular ionic interactions. *J Biol Chem* **274**, 15473-15479 (1999).
10. Vogel V. MECHANOTRANSDUCTION INVOLVING MULTIMODULAR PROTEINS: Converting Force into Biochemical Signals. *Annual Review of Biophysics and Biomolecular Structure* **35**, 459-488 (2006).
11. Qiu Z, Kwon AH, Kamiyama Y. Effects of Plasma Fibronectin on the Healing of Full-Thickness Skin Wounds in Streptozotocin-Induced Diabetic Rats. *Journal of Surgical Research* **138**, 64-70 (2007).
12. Johnson MB*, et al.* Topical Fibronectin Improves Wound Healing of Irradiated Skin. *Sci Rep* **7**, 3876 (2017)

13. Nakamura M, Nishida T, Hikida M, Otori T. Combined effects of hyaluronan and fibronectin on corneal epithelial wound closure of rabbit in vivo. *Curr Eye Res* **13**, 385-388 (1994)
14. Le P. M-TS, Nguyen TH., Vo Van T., Huynh K. In Vitro Cell-Free Synthesis of Fibronectin Fibrils: Their Conformation and Effects on Platelet Function. In: *IFMBE Proceedings* (ed^(eds). 6 edn. Springer, Singapore (2018)
15. Chantre CO*, et al.* Production-scale fibronectin nanofibers promote wound closure and tissue repair in a dermal mouse model. *Biomaterials* **166**, 96-108 (2018)
16. Klebe RJ, Bentley KL, Schoen RC. Adhesive substrates for fibronectin. *J Cell Physiol* **109**, 481-488 (1981)
17. Lin M*, et al.* Adsorption force of fibronectin on various surface chemistries and its vital role in osteoblast adhesion. *Biomacromolecules* **16**, 973-984 (2015).
18. Toworfe GK, Composto RJ, Adams CS, Shapiro IM, Ducheyne P. Fibronectin adsorption on surface-activated poly(dimethylsiloxane) and its effect on cellular function. *J Biomed Mater Res A* **71**, 449-461 (2004).
19. Koenig AL, Gambillara V, Grainger DW. Correlating fibronectin adsorption with endothelial cell adhesion and signaling on polymer substrates. *J Biomed Mater Res A* **64**, 20-37 (2003).
20. Mezzenga R, Mitsi M. The Molecular Dance of Fibronectin: Conformational Flexibility Leads to Functional Versatility. *Biomacromolecules* **20**, 55-72 (2019).
21. Monera OD, Kay CM, Hodges RS. Protein denaturation with guanidine hydrochloride or urea provides a different estimate of stability depending on the contributions of electrostatic interactions. *Protein Sci* **3**, 1984-1991 (1994).
22. García AJ, Vega MaD, Boettiger D. Modulation of Cell Proliferation and Differentiation through Substrate-dependent Changes in Fibronectin Conformation. *Molecular Biology of the Cell* **10**, 785-798 (1999).
23. Lariviere B, Rouleau M, Picard S, Beaulieu AD. Human plasma fibronectin potentiates the mitogenic activity of platelet-derived growth factor and complements its wound healing effects. *Wound Repair Regen* **11**, 79-89 (2003).
24. Liao YX, Zhang ZP, Zhao J, Liu JP. Effects of Fibronectin 1 on Cell Proliferation, Senescence and Apoptosis of Human Glioma Cells Through the PI3K/AKT Signaling Pathway. *Cellular Physiology and Biochemistry* **48**, 1382-1396 (2018).
25. Toledo-Piza AR, Nakano E, Rici RE, Maria DA. Proliferation of fibroblasts and endothelial cells is enhanced by treatment with Phyllocaulis boraceiensis mucus. *Cell Prolif* **46**, 97-108 (2013).
26. Chabria M, Hertig S, Smith ML, Vogel V. Stretching fibronectin fibres disrupts binding of bacterial adhesins by physically destroying an epitope. *Nature Communications* **1**, 135 (2010).
27. Tracy LE, Minasian RA, Caterson EJ. Extracellular Matrix and Dermal Fibroblast Function in the Healing Wound. *Adv Wound Care (New Rochelle)* **5**, 119-136 (2016).

28. Clark RA, Lanigan JM, DellaPelle P, Manseau E, Dvorak HF, Colvin RB. Fibronectin and fibrin provide a provisional matrix for epidermal cell migration during wound reepithelialization. *J Invest Dermatol* **79**, 264-269 (1982).
29. Liang CC, Park AY, Guan JL. In vitro scratch assay: a convenient and inexpensive method for analysis of cell migration in vitro. *Nat Protoc* **2**, 329-333 (2007).
30. Kwon AH, Qiu Z, Hiraon Y. Effect of plasma fibronectin on the incisional wound healing in rats. *Surgery* **141**, 254-261 (2007).
31. Grinnell F, Billingham RE, Burgess L. Distribution of fibronectin during wound healing in vivo. *J Invest Dermatol* **76**, 181-189 (1981).
32. Kochhar R, Kumar N, Singh V, Goenka MK, Mehta SK. Plasma fibronectin levels in patients with idiopathic ulcerative colitis. *Natl Med J India* **4**, 108-110 (1991).
33. Kikuchi T, Hiwatashi N, Goto Y. Plasma fibronectin in inflammatory bowel disease. *Nihon Shokakibyo Gakkai Zasshi* **82**, 599-602 (1985).
34. Luo J-d, Chen AF. Nitric oxide: a newly discovered function on wound healing. *Acta Pharmacologica Sinica* **26**, 259-264 (2005).
35. Futagami A, Ishizaki M, Fukuda Y, Kawana S, Yamanaka N. Wound Healing Involves Induction of Cyclooxygenase-2 Expression in Rat Skin. *Laboratory Investigation* **82**, 1503-1513 (2002).
36. Guo G*, et al.* Anti-inflammatory effects of eriocitrin against the dextran sulfate sodium-induced experimental colitis in murine model. *J Biochem Mol Toxicol* **33**, e22400 (2019).
37. Szymanski JM, Sevcik EN, Zhang K, Feinberg AW. Stretch-dependent changes in molecular conformation in fibronectin nanofibers. *Biomaterials Science* **5**, 1629-1639 (2017).
38. Vadillo-Rodriguez V, Bruque JM, Gallardo-Moreno AM, Gonzalez-Martin ML. Surface-dependent mechanical stability of adsorbed human plasma fibronectin on Ti6Al4V: domain unfolding and stepwise unraveling of single compact molecules. *Langmuir* **29**, 8554-8560 (2013).
39. Bergkvist M, Carlsson J, Oscarsson S. Surface-dependent conformations of human plasma fibronectin adsorbed to silica, mica, and hydrophobic surfaces, studied with use of Atomic Force Microscopy. *J Biomed Mater Res A* **64**, 349-356 (2003).
40. Mozafari MR, Reed CJ, Rostron C. Cytotoxicity evaluation of anionic nanoliposomes and nanolipoplexes prepared by the heating method without employing volatile solvents and detergents. *Pharmazie* **62**, 205-209 (2007).
41. Smistad G, Jacobsen J, Sande SA. Multivariate toxicity screening of liposomal formulations on a human buccal cell line. *Int J Pharm* **330**, 14-22 (2007).
42. Halter M, Antia M, Vogel V. Fibronectin conformational changes induced by adsorption to liposomes. *J Control Release* **101**, 209-222 (2005).
43. Liang C-C, Park AY, Guan J-L. In vitro scratch assay: a convenient and inexpensive method for analysis of cell migration in vitro. *Nature Protocols* **2**, 329-333 (2007).

44. Schoepfer AM, Beglinger C, Straumann A, Trummler M, Renzulli P, Seibold F. Ulcerative colitis: correlation of the Rachmilewitz endoscopic activity index with fecal calprotectin, clinical activity, C-reactive protein, and blood leukocytes. *Inflamm Bowel Dis* **15**, 1851-1858 (2009).

Figures

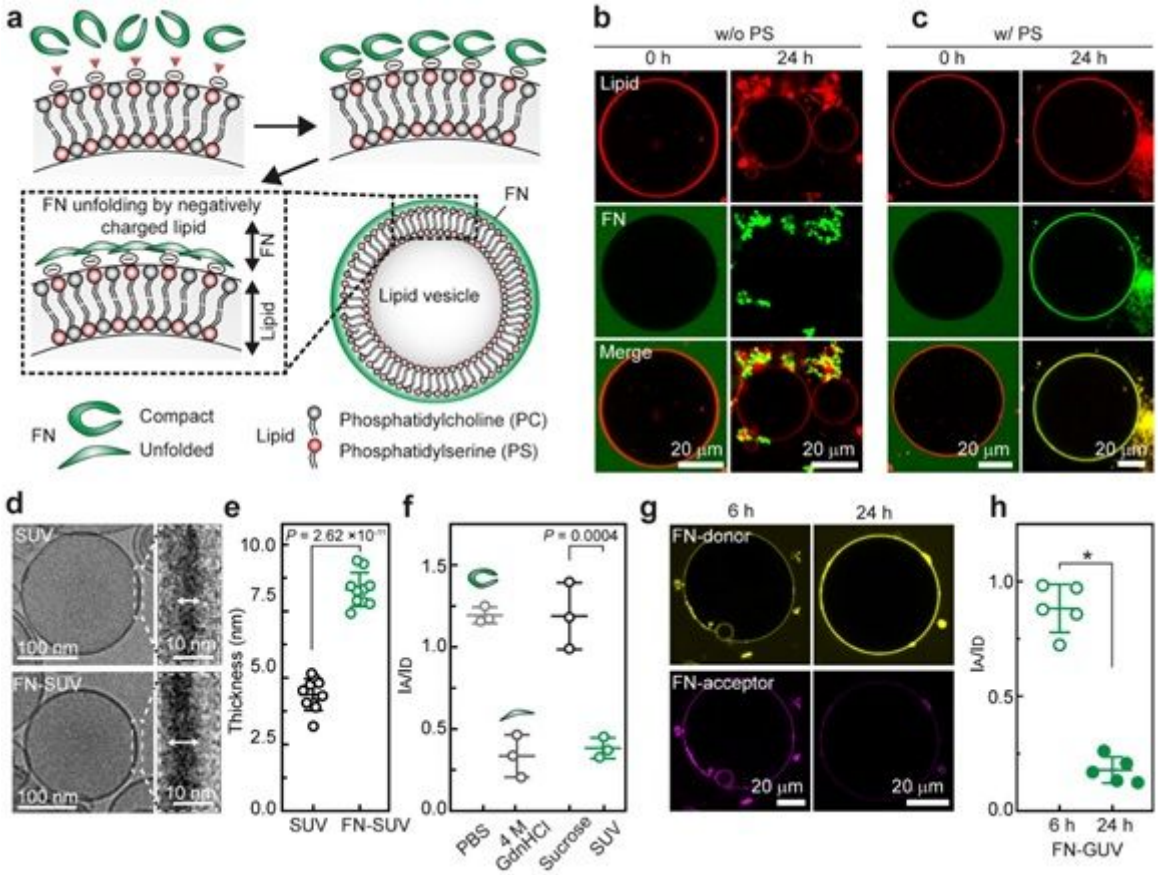

Figure 1

Fibronectin binds to negatively charged vesicles and changes its conformation. a, Illustration showing how a negatively charged surface induces binding and stretching of fibronectin (FN). b, c, Confocal images of a GUV (red) without (b) or with (c) PS after incubation with FN (green) for 24 h (n = 5 independent experiments per group). d, Cryo-TEM images of an SUV and magnified views of its membrane (right panels) after incubation with (lower) or without FN (upper). e, Summary of the membrane thicknesses observed in (d) (n = 10 per group). f, Data from FRET showing the intensity ratio IA/ID observed in double-labeled FN diluted in PBS, 4 M GdnHCl, and sucrose or incubated with SUVs (n = 3 per group). IA and ID are the acceptor and donor fluorescence intensities, respectively. g, Single-vesicle FRET using confocal imaging showing the donor and acceptor intensities in GUVs after 6 h and 24 h of incubation with FN. h, Summary of single-vesicle FRET from (g) showing the intensity ratios IA/ID after 6 h and 24 h of incubation with FN and GUVs (n = 5 per group). Data represent the means ± standard deviations (SDs).

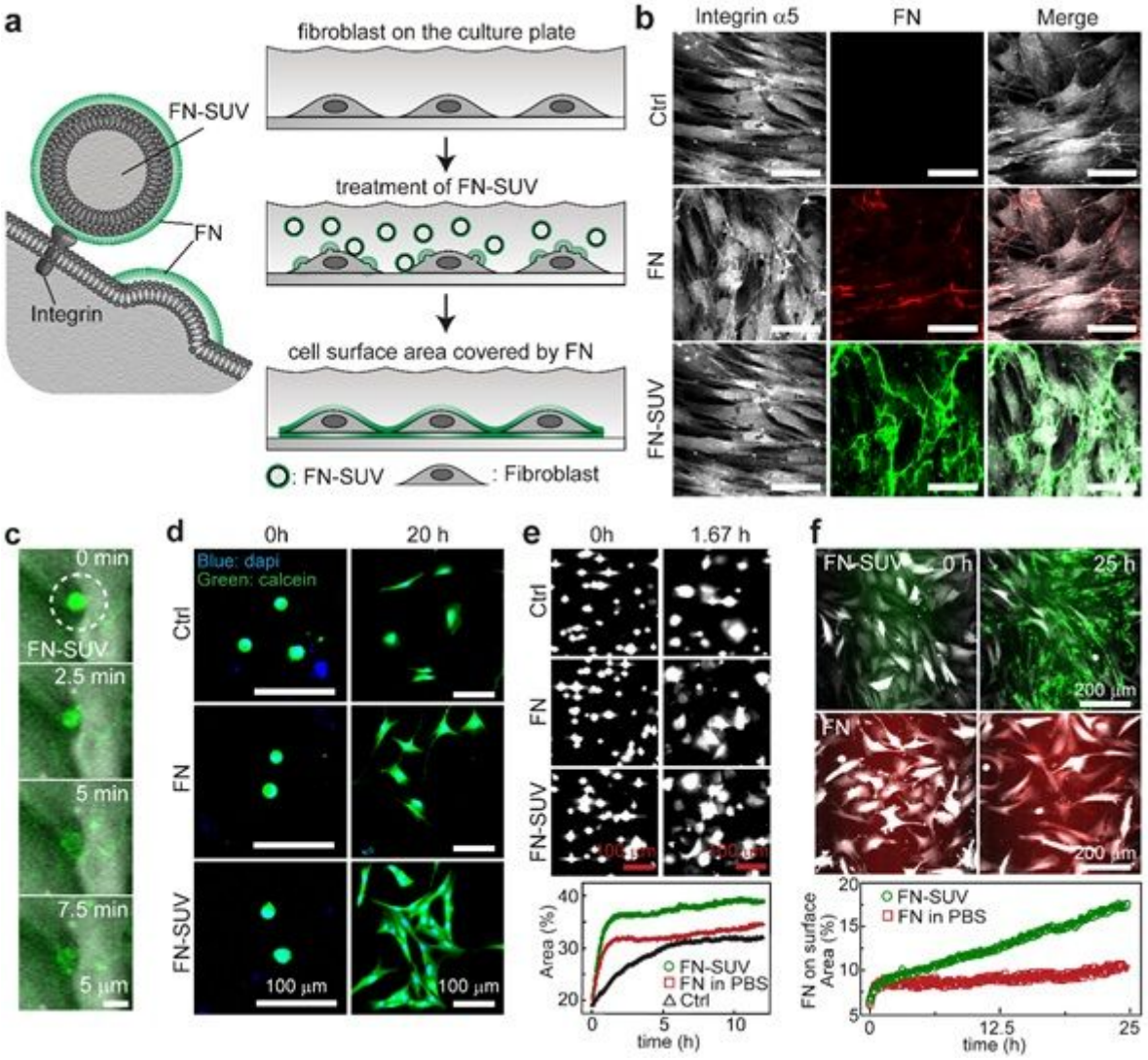

Figure 2

Delivery of FN-SUVs enhances fibrillogenesis and cell attachment. a, Schematics of FN-SUV on the HDFn surface. b, Immunostaining images illustrating binding patterns of FN fibrils (red or green) on HDFn surfaces (n = 3 independent experiments per group). White is integrin α5-FITC antibody. c, Images of 7.5-min time intervals showing the untangling process of FN-SUV bundles on the surfaces of HDFn cells (n = 3). d, Live-cell images showing changes in the morphologies of HDFn cells after 20 h of incubation with PBS (Ctrl), FN or FN-SUVs (n = 3 independent experiments per group). e, Attachment rate of HDFn cells quantified by the area of the cells attached to the dish's surface (n = 3 per group). f, Live cell images showing the areas of the FN matrix formed on the surfaces of HDFn cells after incubation with FN or FN-SUVs (n = 3 independent experiments per group).

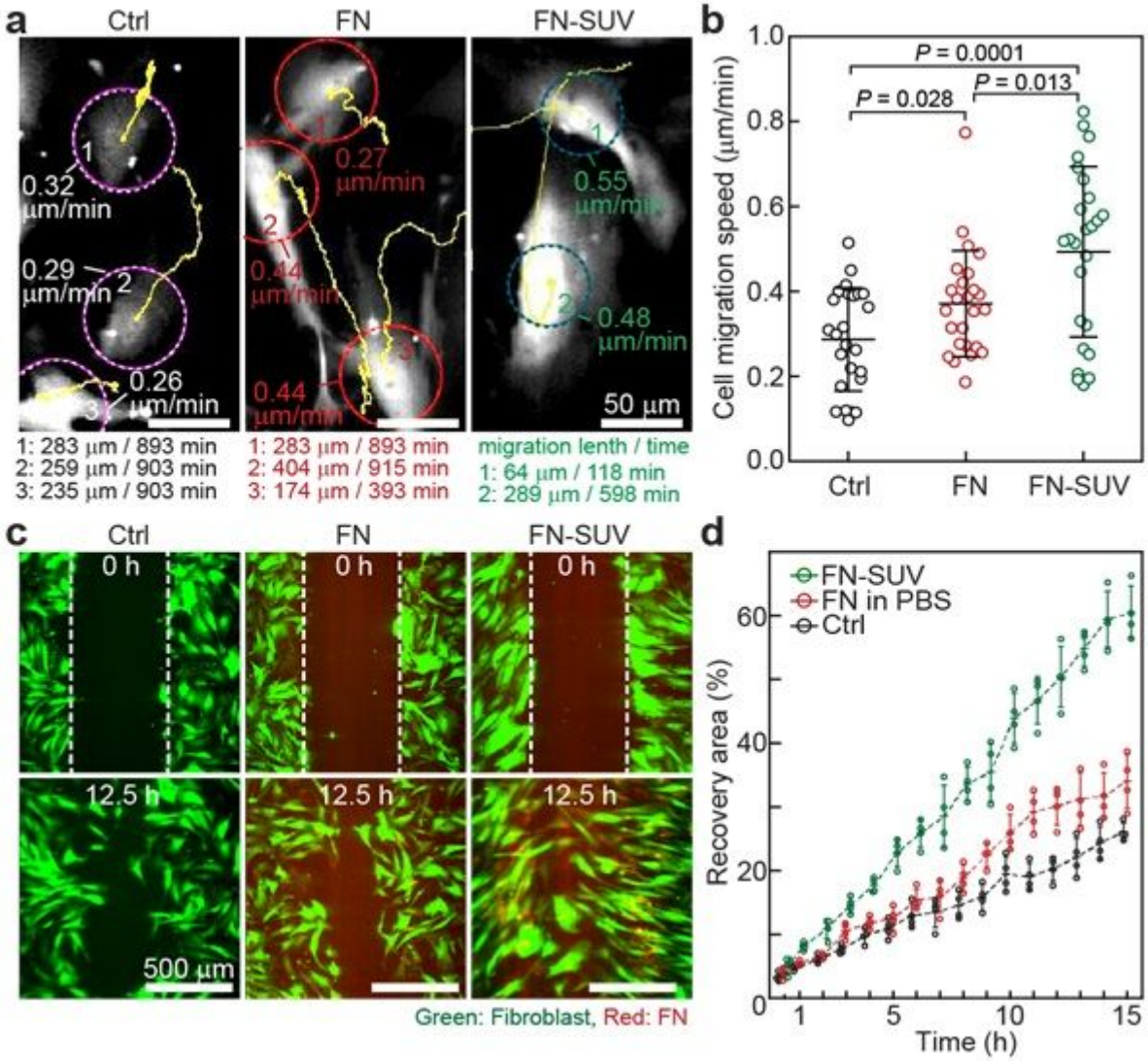

Figure 3

FN-SUV treatment accelerates the migration rate of HDFn cells. a, Representative images tracking the migration speed of single HDFn cells in the control (Ctrl), FN- and FN-SUV-treated groups. b, Summary of the single-cell migration speeds in the control, FN- and FN-SUV-treated HDFn cells (n = 25, from 5 independent experiments). c, In vitro scratch assays were performed in the control, FN- and FN-SUV-treated HDFn cells to compare the rates of migration. Representative images were extracted from the time series at 0 and 12.5 h. d, Results of quantitative analyses of the recovery areas covered by migrated cells as described in (c). Data were collected from the same optical field at 1-hour time intervals over 15 h (n = 4 independent experiments).

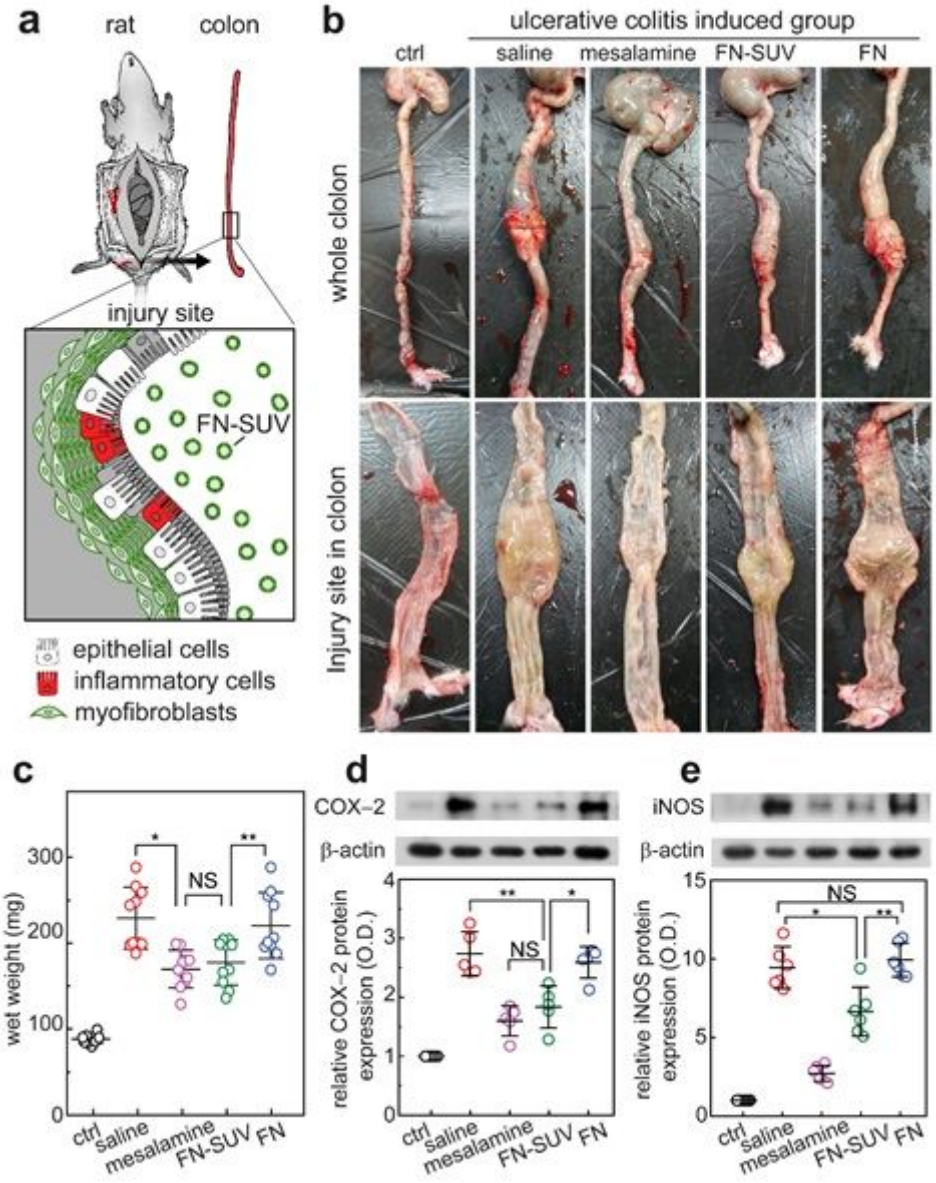

Figure 4

FN-SUV treatment improves the healing process of acid-induced ulcers in rat colons. a, Hypothesized schematic of FN-SUV treatment in the rat colon. b, Gross morphologies of the intestines removed from the rats after 10 days of treatment. In the control group, the healthy colon wall is thin and smooth with no mucus. In the colitis-induced groups, the wall of the colon is swollen and filled with blood and mucus. Various degrees of colitis can be seen among the different treatments. c, Colon wet weight of the control and colitis-induced groups as described in (a) (n = 10 per group). P values were calculated using Student's t tests. d, e, Expression levels of the inflammatory indicators COX-2 (n = 5 per group) (c) and iNOS (n = 6 per group) (d). P values were calculated using one-way ANOVA. c, *P = 0.0003, **P = 0.009. d, *P = 0.0006, **P = 0.0034. e, *P = 0.0009, **P = 0.0001. c-e, Error bars indicate mean ± SDs.

Supplementary Files

This is a list of supplementary files associated with this preprint. Click to download.

- S1ZstackbindingtestofS.aureustoCOL.mp4
- S2ZstackbindingtestofS.aureustoFN.mp4
- S3ZstackbindingtestofS.aureustopureGUV.mp4
- S4migrationFNV.mp4
- S5TrackMatemigrationcontrollabel.mp4
- S6TrackMatemigrationFNlabel.mp4
- S7TrackMatemigrationFNVlabel.mp4
- S8Scratchtestctrl.mp4
- S9ScratchtestFN.mp4
- S10ScratchtestFNvesicle.mp4
- S11DICfibroblastFNV.mp4
- WoundHealingSupplementaryInfoNatCommformatHuong.docx